PHYSICAL REVIEW A VOLUME 45, NUMBER 6 15 MARCH 1992

Fast and slow sound in a dense gas mixture of helium and neon

P. Westerhuijs, W. Montfrooij,* L. A. de Graaf, and I. M. de Schepper
Interfaculty Reactor Institute, Delft University of Technology, 2629 JB Delft, The Netherlands

(Received 21 August 1991)

For a dense gas equilibrium mixture of 65 at. % He and 35 at. % Ne at $T=39.3$ K and $p=114$ bar, we determine from neutron scattering the total dynamic structure factor $S(k,\omega)$ as a function of frequency ω for wave numbers $4<k<28\ \mathrm{nm}^{-1}$. For all k, $S(k,\omega)$ is a sum of four Lorentzians; two located at $\omega=\pm\omega_s^{(1)}(k)$ (directly visible for smaller k) and two located at $\omega=\pm\omega_s^{(2)}(k)$ (not visible). $\omega_s^{(1)}(k)>ck$ can be attributed to fast oscillations of the light He particles (fast sound) and $\omega_s^{(2)}(k)<ck$ to slow oscillations of the heavy Ne particles (slow sound), where c is the hydrodynamic ($k\to 0$) sound velocity of the total mixture. $\omega_s^{(1)}(k)$ is virtually indistinguishable from the (extended) sound dispersion measured in pure helium at $T=39.3$ K and $p=114$ bar. A kinetic model, consistent with our experiment, predicts that fast sound vanishes at $k=0.7\ \mathrm{nm}^{-1}$ and that slow sound merges into hydrodynamic sound then.

PACS number(s): 61.12.−q, 05.20.−y, 61.20.Lc

I. INTRODUCTION

Recent theoretical calculations [1,2] and molecular-dynamics (MD) simulations [3,4] on disparate-mass binary fluid mixtures in equilibrium have shown that in the partial dynamic structure factor $S_{11}(k,\omega)$ of the light component (1) side peaks occur at the frequencies $\omega=\pm\omega_s^{(1)}(k)$ for wave numbers k beyond the hydrodynamic regime ($k>k_H$, with k_H the limiting hydrodynamic wave number). Since $\omega_s^{(1)}(k)>ck$, with c the hydrodynamic speed of sound, the side peaks in $S_{11}(k,\omega)$ are attributed to fast oscillations supported by the light particles alone (fast sound). It appears that for $k>k_H$, the heavy particles (2) cannot follow the oscillations of the light particles, a new effect not seen in hydrodynamics ($k<k_H$), where the constituents oscillate simultaneously so that c is determined by *both* components of the mixture. Indeed, for $k>k_H$, no side peaks at $\pm\omega_s^{(1)}(k)$ occur in the partial dynamic structure factor $S_{22}(k,\omega)$ of the heavy component. Instead, $S_{22}(k,\omega)$ shows side features at $\omega=\pm\omega_s^{(2)}(k)$, i.e., either very weak shoulders [3] or (not directly visible) Lorentzians obtained from line fitting [1,2,4]. The frequency $\omega_s^{(2)}(k)<ck$ is attributed to slow oscillations due mainly to the heavy particles (slow sound). Thus both theory and MD predict that for binary mixtures the hydrodynamic ($k<k_H$) sound dispersion $\omega_s(k)=ck$ will split up for increasing $k>k_H$ into two branches: fast sound $\omega_s^{(1)}(k)>ck$ and slow sound $\omega_s^{(2)}(k)<ck$.

The total dynamic structure factor $S(k,\omega)$ measured by neutron scattering [5] on a dense gas mixture of 65 at. % He and 35 at. % Ne at temperature $T=39.3$ K and pressure $p=114$ bar shows clear side peaks or shoulders at $\omega_s^{(1)}(k)>ck$, in agreement with the predicted existence of a fast-sound mode in mixtures. A series of light-scattering experiments on dilute gas mixtures has shown the existence of both fast and slow sound [6,7]. In this paper we give a more-detailed account of the neutron-scattering experiment reported in Ref. [5]. In particular, we show that $S(k,\omega)$ can be described very well by a sum of four Lorentzians located at $\pm\omega_s^{(1)}(k)$ [with $\omega_s^{(1)}(k)>ck$] and $\pm\omega_s^{(2)}(k)$ [with $\omega_s^{(2)}(k)<ck$]. The two directly visible Lorentzians at $\pm\omega_s^{(1)}(k)$ are almost certainly due to fast oscillations of the light He particles, since $\omega_s^{(1)}(k)$ agrees perfectly with the extended sound dispersion $\omega_s(k)$ obtained from a recent neutron-scattering experiment [8] on a corresponding pure-He state at $T=39.3$ K and $p=114$ bar. We argue that the two (not directly visible) Lorentzians of the He-Ne mixture, located at $\pm\omega_s^{(2)}(k)$, are most likely due to slow oscillations of the heavy Ne particles. The reason is that the two Lorentzians at $\pm\omega_s^{(2)}(k)$ determine the half width at half height $\omega_H(k)$ of the total $S(k,\omega)$, and that the observed behavior of $\omega_H(k)$ can be understood from the dynamics of the Ne atoms in the He-Ne mixture. We find that all observed wave numbers $4<k<28\ \mathrm{nm}^{-1}$ are beyond the hydrodynamic regime, i.e., $k>k_H$. The most obvious difference between hydrodynamic predictions and our present results is that in hydrodynamics ($k<k_H$) $S(k,\omega)$ is described by two (different) *central* Lorentzians (due to heat and mutual particle diffusion) and two Lorentzians located at $\omega=\pm ck$ (due to hydrodynamic sound propagation) [9]. To make a connection between the two k regions, we present a kinetic model that is consistent with our experimental $S(k,\omega)$ for $k>k_H$ and can be extended to $k<k_H$. This model predicts that $k_H=0.7\ \mathrm{nm}^{-1}$, where fast sound vanishes and slow sound merges into hydrodynamic sound.

This paper is organized as follows. In Sec. II we give the details of the neutron-scattering experiment from which the total $S(k,\omega)$ of the He-Ne mixture is determined. In Sec. III we present the results derived from $S(k,\omega)$ either directly or indirectly (by Lorentzian line fitting). In Sec. IV we discuss the kinetic model that extends the results to hydrodynamics. We end with a discussion in Sec. V. Throughout we use the results of the neutron-scattering experiment on pure helium [8] as a reference for the behavior of the light component (He) in our He-Ne mixture.

II. EXPERIMENT

Our neutron-scattering experiment on the He-Ne mixture was performed on the rotating-crystal spectrometer RKS2 at the Interfaculty Reactor Institute in Delft. The monochromatic incident beam of neutrons on the He-Ne sample had a cross section of 2.5×10 cm^2 and an intensity of $I_0=800$ neutrons/cm^2 s. The wavelength $\lambda_0=0.200$ nm of the neutrons in the incident beam was selected by a rotating pyrolytic graphite crystal (18750 rpm) and using the (004) Bragg reflection (Bragg angle $\theta_B=36.6°$). The sample container was a single aluminum cylinder with length 11 cm, diameter 2 cm, and wall thickness 0.1 cm subdivided into six parts, with disks of boron nitride (a pure absorber) to reduce multiple scattering. This container was filled at $T=39.3$ K first with pure ^{4}He up to a pressure $p=83$ bar and then with purified natural Ne up to a total pressure $p=114$ bar. The number densities n_1 of He and n_2 of Ne of the resulting He-Ne sample are $n_1=12.1$ nm^{-3} (derived from Ref. [10]) and $n_2=6.5$ nm^{-3} (derived from a mass-spectroscopy measurement on the total sample). We note that this value of n_2 differs from the estimate $n_2=3$ nm^{-3} reported in Ref. [5], which was derived from ideal mixing rules.

Spectra $I(\phi,\omega)$ as a function of scattering angle ϕ and energy-gain or -loss frequency ω were obtained from the measured intensity of scattered neutrons and their time of flight from the sample to the detectors. We used 56 detectors located at a distance 1.503 m from the sample at angles $-17.6°\le\phi\le 69.3°$, with $|\phi|\ge 4.4°$. The experiment was done in four steps, each step taking about 200 h. First, the He-Ne scattering was measured. The total scattering of the He-Ne sample was 5% so that, also due to the boron nitride disks, we can safely neglect the effect of multiply scattered neutrons in the sample. Second, to account for background and the shielding of the container by the sample, the empty container was filled with a very small amount of ^{3}He gas (a pure and strong absorber) that absorbs as many neutrons as the He-Ne sample scatters. Thus, the background spectra $I_B(\phi,\omega)$ are obtained in a manner similar to the determination of the spectra $I(\phi,\omega)$. Third, to account for frequency resolution and absolute normalization, the empty container was filled with vanadium foil for which the scattering properties are known, yielding the spectra $I_{\mathrm{v}}(\phi,\omega)$. Finally, the empty container is filled again with ^{3}He gas to determine the background spectra $I_{B,\mathrm{v}}(\phi,\omega)$ relevant for $I_{\mathrm{v}}(\phi,\omega)$. From the difference $I_{\mathrm{v}}(\phi,\omega)-I_{B,\mathrm{v}}(\phi,\omega)$ we determine the resolution function of the spectrometer. The half width at half height of the resolution functions is $\Delta\omega_R=0.95$ ps^{-1}. The difference $I_{\mathrm{v}}(\phi,\omega)-I_{B,\mathrm{v}}(\phi,\omega)$ is also used as a standard for absolute normalization of $I(\phi,\omega)-I_B(\phi,\omega)$. The spectra $I(\phi,\omega)-I_B(\phi,\omega)$ are further corrected for detector efficiency and the resolution of the spectrometer and interpolated from constant ϕ to constant k using standard correction procedures [11]. Finally, the spectra are symmetrized in ω using the quasiclassical approximation [11]. The size of the error in the spectra so obtained will in general depend on k and ω due to different detector efficiencies (which depend on ϕ), the subtraction of the background (which depends on ϕ and ω), and the interpolation from constant ϕ to constant k.

Thus we obtain the absolutely normalized symmetric total dynamic structure factor $S(k,\omega)$ of the He-Ne mixture, given by

$$S(k,\omega)=x_1b_1^{*2}S_{11}(k,\omega)+x_2b_2^{*2}S_{22}(k,\omega)+2(x_1x_2)^{1/2}b_1^*b_2^*S_{12}(k,\omega)\ , \tag{2.1}$$

with $x_1=n_1/(n_1+n_2)=0.65$ the number concentration of He, $x_2=n_2/(n_1+n_2)=0.35$ the number concentration of Ne, and b_j^* the normalized scattering length of species j, i.e.,

$$b_j^*=b_j/(x_1b_1^2+x_2b_2^2)^{1/2}\ , \tag{2.2}$$

with $b_1=3.26$ fm the scattering length of He and $b_2=4.55$ fm the scattering length of Ne, so that $x_1b_1^{*2}=0.49$, $x_2b_2^{*2}=0.51$, and $2(x_1x_2)^{1/2}b_1^*b_2^*=1.00$. In Eq. (2.1) the $S_{jl}(k,\omega)$ are the partial dynamic structure factors given by

$$S_{jl}(k,\omega)=\frac{1}{2\pi}\int_{-\infty}^{\infty}dt\, e^{i\omega t}F_{jl}(k,t)\ , \tag{2.3}$$

with j or $l=1,2$, and the $F_{jl}(k,t)$ are the intermediate partial scattering functions

$$F_{jl}(k,t)=\langle[\delta n_j(\mathbf{k},0)]^*\delta n_l(\mathbf{k},t)\rangle\ . \tag{2.4}$$

Here the angular brackets denote the equilibrium canonical ensemble average, the asterisk denotes complex conjugation, $\mathbf{k}$ is a wave vector with length k, and $\delta n_l(\mathbf{k},t)$ is a microscopic plane-wave density fluctuation of species $l=1$ or 2 at time t, given for $\mathbf{k}\neq\mathbf{0}$ by

$$\delta n_l(\mathbf{k},t)=\frac{1}{\sqrt{N_l}}\sum_{p=1}^{N_l}e^{i\mathbf{k}\cdot\mathbf{r}_l^{(p)}(t)}\ , \tag{2.5}$$

with N_l the number of particles of species l and $\mathbf{r}_l^{(p)}(t)$ the position of particle p of species l at time t. We refer to $S_{11}(k,\omega)$ in Eq. (2.1) as the He contribution (describing the dynamics of the He density fluctuations in the mixture), to $S_{22}(k,\omega)$ as the Ne contribution, and to $S_{12}(k,\omega)$ as the cross term (describing the influence of He fluctuations on Ne fluctuations and vice versa). The results for the total $S(k,\omega)$ [cf. Eq. (2.1)] are presented in the next section.

III. RESULTS

In this section we present the results of our neutron-scattering experiment on the 65% He and 35% Ne mixture at $T=39.3$ K and $p=114$ bar. As a reference, we compare the data for the He-Ne mixture with results obtained from a neutron-scattering experiment [8] on pure He at $T=39.3$ K, $p=114$ bar, and number density [10] $n=15.1$ nm^{-3}. The dynamic structure factor $S(k,\omega)$ of pure He is given by expressions equivalent to Eqs. (2.1)–(2.5) with $x_1=1$ and $x_2=0$. For both fluids we present and discuss $S(k,\omega)$ Sec. (III A), their areas Sec. (III B), second-frequency moments Sec. (III C), half widths Sec. (III D), and the results obtained from Lorentzian line fitting (Sec. III F).

A. Dynamic structure factor

In Fig. 1(a) we show the total $S(k,\omega)$ of the He-Ne mixture [cf. Eq. (2.1)] as a function of ω for wave numbers $k=5$, 6, 7 and 8 nm^{-1}. One observes clearly visible side peaks in $S(k,\omega)$ at frequencies we shall call $\omega_s^{(1)}(k)$. In Fig. 1(b) we display the $S(k,\omega)$ of pure He at the same values $k=5$, 6, 7 and 8 nm^{-1}. One finds (in fact, for all k) that the $S(k,\omega)$ of pure He are rather featureless, do not show any side wings (cf. Fig. 1), and therefore appear quite different from the $S(k,\omega)$ of the He-Ne mixture. [In Fig. 1(b) we only show the error in $S(k,\omega)$, averaged over ω.] In Fig. 2 we show the $S(k,\omega)$ of the He-Ne mixture for wave numbers $k=9,10,\ldots,20$ nm^{-1}. Side wings or shoulders in $S(k,\omega)$ can still be observed at finite frequencies $\omega_s^{(1)}(k)$ (albeit barely for most k values).

B. Static structure factor

Next we consider the areas of $S(k,\omega)$, i.e., the static structure factors $S(k)$ given by

$$S(k)=\int_{-\infty}^{\infty} d\omega\, S(k,\omega)\,, \tag{3.1}$$

so that for the He-Ne mixture [cf. Eq. (2.1)],

$$S(k)=x_1 b_1^{*2} S_{11}(k)+x_2 b_2^{*2} S_{22}(k) +2(x_1 x_2)^{1/2} b_1^* b_2^* S_{12}(k)\,, \tag{3.2}$$

where the partial structure factor $S_{jl}(k)$ is the area of $S_{jl}(k,\omega)$.

In Fig. 3 we plot $S(k)$ of the He-Ne mixture and of the pure-He state. Both $S(k)$ are very similar and appear to be hard-sphere-like. For pure He we find a best fit with the theoretical Percus-Yevick hard-sphere $S(k)$ [12] when we take $\sigma_1=0.248$ nm as the equivalent hard-sphere diameter of the He particles (cf. Fig. 3). Using this value $\sigma_1=0.248$ nm for the helium particles, we find a best fit of the $S(k)$ of the He-Ne mixture with the Percus-Yevick hard-sphere $S(k)$ of mixtures when we take $\sigma_2=0.288$ nm as the equivalent hard-sphere diameter of the Ne particles (cf. Fig. 3). According to the Percus-Yevick theory, the static structure factor $S(k)$ of a mixture depends only on n_1, σ_1, b_1, and n_2, σ_2, and b_2. Since σ_2/σ_1 is close to 1, the $S(k)$ of the He-Ne mixture is very similar to that of a pure fluid with number density n_1+n_2 and particles of size $\sigma_1 \approx \sigma_2$, i.e., roughly to that of pure He (cf. Fig. 3). The large difference between the He mass m_1 and Ne mass m_2 ($m_2/m_1=5$) is irrelevant to understand $S(k)$. As a further consequence of this theory, the contribution to the total $S(k)$ in Eq. (3.2) of the helium particles $[\sim S_{11}(k)]$ and neon particles $[\sim S_{22}(k)]$ in the He-Ne mixture is about equal for all k. The cross term $[\sim S_{12}(k)]$ contributes considerably less to $S(k)$ than the He or Ne term.

C. Second-frequency moment

The reduced second-frequency moment $M_2(k)$ of $S(k,\omega)$ is defined by

$$M_2(k)=\int_{-\infty}^{\infty} d\omega (\omega/k)^2 S(k,\omega)\,, \tag{3.3}$$

and is therefore typical for the large-ω behavior of $S(k,\omega)$. In Fig. 4 we display the experimental $M_2(k)$ of the He-Ne mixture and of pure He, where one sees that $M_2(k)$ of He-Ne is considerably smaller than $M_2(k)$ of He. The theoretical value of $M_2(k)$ for the He-Ne mixture is given by [cf. Eqs. (2.1)–(2.5)]

$$M_2(k)=x_1 b_1^{*2}(\beta m_1)^{-1}+x_2 b_2^{*2}(\beta m_2)^{-1}\,, \tag{3.4}$$

with $\beta=(k_B T)^{-1}$. Here $(\beta m_1)^{-1}$ and $(\beta m_2)^{-1}$ are the reduced second-frequency moments of the helium contribution $S_{11}(k,\omega)$ and neon contribution $S_{22}(k,\omega)$ to $S(k,\omega)$ in Eq. (2.1), respectively. The reduced second-frequency moment of the cross term $S_{12}(k,\omega)$ in Eq. (2.1) vanishes. Thus [cf. Eq. (3.4)] $M_2(k)=0.49(\beta m_1)^{-1}+0.51(\beta m_2)^{-1}=0.048\ \mathrm{nm}^2\,\mathrm{ps}^{-2}$, agreeing reasonable well with the experimental values. Due to the large mass ratio $m_2/m_1=5$, 83% of the theoretical $M_2(k)$ is contributed by the first term $0.49(\beta m_1)^{-1}$, i.e., by the light helium component in the mixture. This implies that the *large-ω* behavior of the total $S(k,\omega)$ of the He-Ne mixture is strongly dominated by the contribution of the *helium* particles. The theoretical value of $M_2(k)$ for the pure-He state is $M_2(k)=(\beta m_1)^{-1}=0.0816$

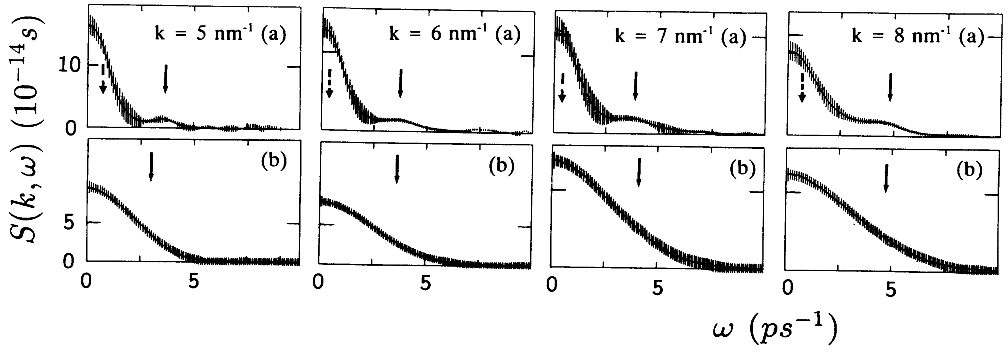

FIG. 1. Dynamic structure factors $S(k,\omega)$ (error bars) of (a) $\mathrm{He}_{0.65}\mathrm{Ne}_{0.35}$ and (b) pure He both at 39.3 K and 114 bar as a function of ω. Solid curves are the best Lorentzian line fits with (a) four and (b) three lines. Arrows point to the frequency $\omega_s^{(2)}(k)$ of slow sound [dashed arrow in (a)], $\omega_s^{(1)}(k)$ of fast sound [solid arrow in (a)], and $\omega_s(k)$ of normal extended sound [solid full arrow in (b)]. Note that $\omega_s^{(1)}(k) \approx \omega_s(k)$, and that the half width for pure He [in (b)] is much larger than for $\mathrm{He}_{0.65}\mathrm{Ne}_{0.35}$ [in (a)].

$\mathrm{nm}^2\,\mathrm{ps}^{-2}$ (cf. Fig. 4), also in agreement with experiment. Therefore, the large increase in $M_2(k)$ from the He-Ne mixture to the pure-He state (cf. Fig. 4) is due to the fact that mainly the He particles in the mixture contribute to $M_2(k)$, while there are fewer He particles per unit volume in the mixture than in the pure-He state. As a consequence of these results, the total $S(k,\omega)$ of the He-Ne mixture is dominated for *small* ω by the *neon* contribution; since $S_{11}(k,\omega)$ and $S_{22}(k,\omega)$ in Eq. (2.1) have about equal area, $S_{11}(k,\omega)>S_{22}(k,\omega)$ for large ω, so that $S_{11}(k,\omega)<S_{22}(k,\omega)$ for small ω.

D. Half width

The quantity most typical to characterize the small-ω behavior of $S(k,\omega)$ is the half width at half height $\omega_H(k)$, defined by

$$S(k,\omega_H(k))=\tfrac{1}{2}S(k,0)\ . \tag{3.5}$$

In Fig. 5 we plot $\omega_H(k)$ for the pure-He state and for the He-Ne mixture. One observes that $\omega_H(k)$ of pure He is for all k considerably larger than $\omega_H(k)$ of the mixture, as can also be seen directly in Fig. 1. To understand, globally, the behavior of $\omega_H(k)$ of pure He, we consider the equivalent fluid of hard spheres with diameter $\sigma_1=0.248$ nm. For this pure fluid of hard spheres, the mean free path between collisions is $l=0.175$ nm. Then, for large wave numbers $k\gg l^{-1}$, one might expect that $S(k,\omega)$ is determined by the free motion of the He particles, so that $S(k,\omega)$ is Gaussianlike in ω with area $S(k)$ and reduced second-frequency moment $(\beta m_1)^{-1}$. Therefore, using this Gaussian shape of $S(k,\omega)$, the half width $\omega_H(k)$ of pure He should be approximately given by

$$\omega_H^{(1)}(k)=k[\beta m_1 S(k)]^{-1/2}\ . \tag{3.6}$$

In Fig. 5 we also show $l^{-1}=5.7\ \mathrm{nm}^{-1}$ (arrow) and $\omega_H^{(1)}(k)$, with $S(k)$ taken from the Percus-Yevick theory [cf. Fig. 3(a)]. The half widths $\omega_H(k)$ and $\omega_H^{(1)}(k)$ of pure He indeed agree well for $k>l^{-1}$ (cf. Fig. 5), meaning that free motion is the physical process most relevant to understand $S(k,\omega)$ for $k\gg l^{-1}$.

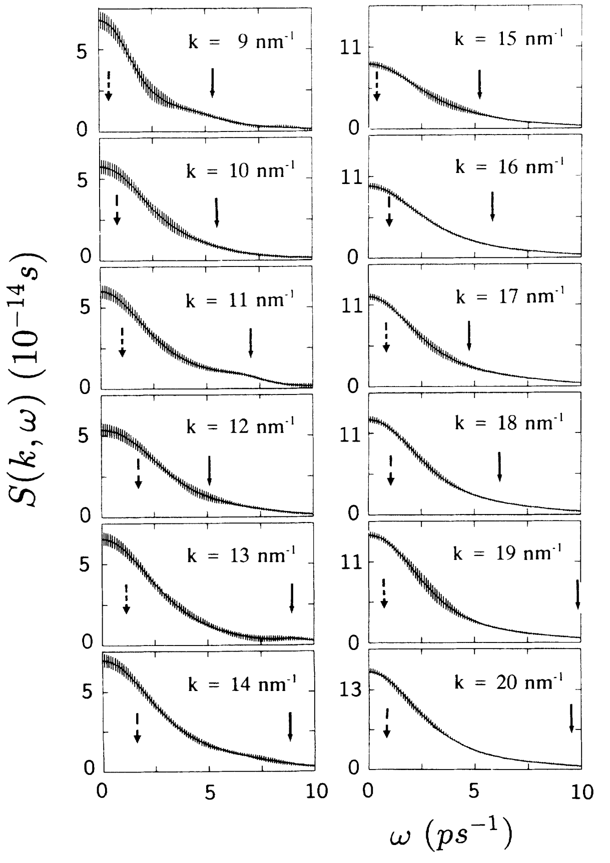

FIG. 2. Dynamic structure factors $S(k,\omega)$ (error bars) of $\mathrm{He}_{0.65}\mathrm{Ne}_{0.35}$ at 39.3 K and 114 bar as a function of ω. Solid curves are the best four-Lorentzian line fits. Arrows point to the frequencies $\omega_s^{(2)}(k)$ of slow sound (dashed arrow) and $\omega_s^{(1)}(k)$ of fast sound (solid arrow).

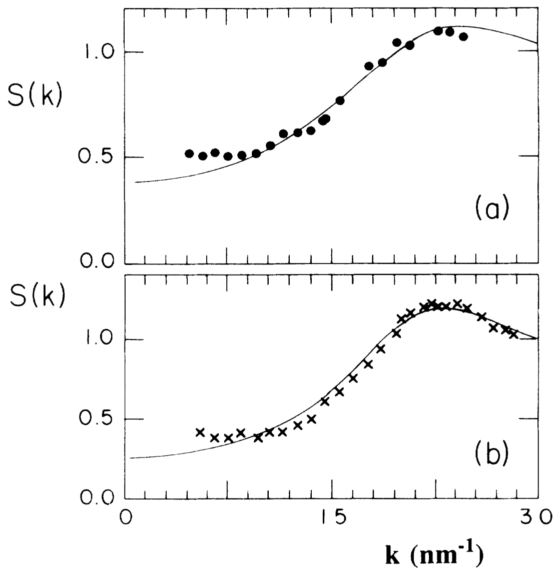

FIG. 3. Static structure factors $S(k)$ as a function of k for pure He [closed circles in (a)] and for $\mathrm{He}_{0.65}\mathrm{Ne}_{0.35}$ [crosses in (b)] both at 39.3 K and 114 bar. Solid curves are theoretical for corresponding hard-sphere fluids.

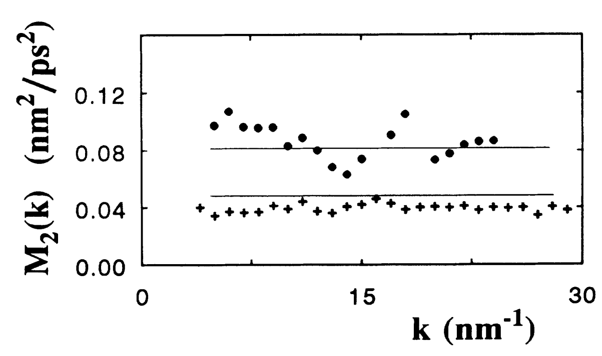

FIG. 4. Reduced second-frequency moment $M_2(k)$ as a function of k for pure He (closed circles from experiment, upper solid curve from theory) and for $\mathrm{He}_{0.65}\mathrm{Ne}_{0.35}$ [crosses from experiment, lower solid curve from theory, cf. Eq. (3.4)].

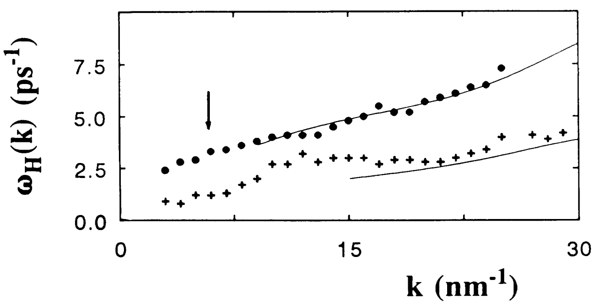

FIG. 5. Half width $\omega_H(k)$ as a function of k for pure He [closed circles from experiment, upper solid curve from Eq. (3.6)] and for $He_{0.65}Ne_{0.35}$ [crosses from experiment, lower solid curve from Eq. (3.7)]. The arrow points to $k=l^{-1}$.

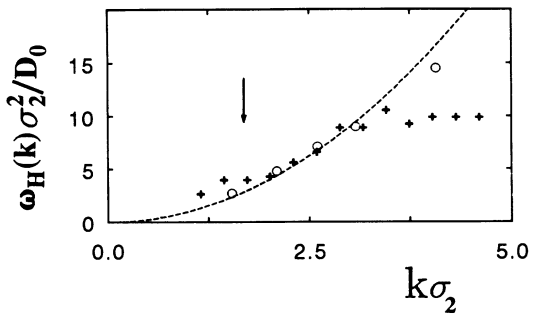

FIG. 6. Reduced half widths $\omega_H(k)\sigma_2^2/D_0$ as a function of reduced wave number $k\sigma_2$ for $He_{0.65}Ne_{0.35}$ (crosses, $\sigma_2=0.288$ nm, $\sigma_2^2/D_0=3.3$ ps), for latex in benzene (open circles, $\sigma_2=219$ nm, $\sigma_2^2/D_0=16$ ms), and $\omega_H(k)=D_0k^2$ (dashed curve, Stokes-Einstein). The arrow points to $k=l^{-1}$.

To understand $\omega_H(k)$ of the He-Ne mixture, we assume that $\omega_H(k)$ is determined fully by the neon contribution $S_{22}(k,\omega)$ in Eq. (2.1) and distinguish two k regions: $k\approx l^{-1}$ and $k\gg l^{-1}$ (with $l=0.175$ nm as a typical length for the averaged mean free path also in the mixture). For $k\gg l^{-1}$, $S_{22}(k,\omega)$ will be Gaussianlike with area $S_{22}(k)$ and reduced second-frequency moment $(\beta m_2)^{-1}$, since the Ne particles can be expected to move freely then. Thus, the half width is approximately given by

$$\omega_H^{(2)}(k)=k[\beta m_2 S_{22}(k)]^{-1/2} . \tag{3.7}$$

We show $\omega_H^{(2)}(k)$ in Fig. 5, with $S_{22}(k)$ taken from the Percus-Yevick theory for hard-sphere mixtures ($\sigma_1=0.248$ nm and $\sigma_2=0.288$ nm). The agreement of $\omega_H^{(2)}(k)$ [cf. Eq. (3.7)] with the experimental half widths $\omega_H(k)$ of the He-Ne mixture, seen in Fig. 5 for $k\gg l^{-1}$, is good enough to ascertain that, indeed, the heavy, free-moving Ne particles determine the relatively small half widths $\omega_H(k)$ of the mixture.

For $k\approx l^{-1}$, we assume that $S_{22}(k,\omega)$ is determined by a diffusivelike motion of the Ne particles through a fluid of He as if the He-Ne mixture were a colloidal suspension, with Ne as the colloidal particles and He as the solvent. For colloidal suspensions, it is found [13–15] both theoretically and experimentally that the reduced half width $\omega_H(k)\sigma_2^2/D_0$ of the dynamic structure factor $S_{22}(k,\omega)$ of the colloidal particles (labeled 2) is a function only of the reduced wavenumber $k\sigma_2$ and reduced density $n_2\sigma_2^3$, where $D_0=(3\pi\beta\eta\sigma_2)^{-1}$ is the (Stokes-Einstein) diffusion coefficient of a single colloidal particle in the solvent, with η the shear viscosity of the solvent. In Fig. 6 we plot for the He-Ne mixture and $4\leq k\leq 15$ nm^{-1} the reduced half width $\omega_H(k)\sigma_2^2/D_0$ as a function of $k\sigma_2$, with $\sigma_2=0.288$ nm, reduced density $n_2\sigma_2^3=0.15$, $D_0=(3\pi\beta\eta\sigma_2)^{-1}=2.51\times10^{-8}$ m^2/s and $\sigma_2^2/D_0=3.3$ ps. Here η is the shear viscosity of the solvent, i.e., of the pure-He fluid [16] ($T=39.3$ K, $p=114$ bar, $\eta=7.9\times10^{-6}$ N s/m^2). In Fig. 6 we also plot the experimental reduced halfwidths $\omega_H(k)\sigma_2^2/D_0$ as a function of $k\sigma_2$ for a real colloidal suspension [15] at virtually the same reduced density $n_2\sigma_2^3=0.14$ i.e., for a suspension of latex balls (diameter $\sigma_2=219$ nm) in benzene at room temperature, for which $D_0=3.0\times10^{-12}$ m^2/s and $\sigma_2^2/D_0=16$ ms. The agreement between the reduced half widths $\omega_H(k)$ of Ne in He and $\omega_H(k)$ of latex spheres in benzene is good for $k\sigma_2<3$ (cf. Fig. 6). Thus, we conclude that the small-ω behavior of the total $S(k,\omega)$ observed in our He-Ne mixture (cf. Figs. 1 and 2) can be attributed to the motion of the neon particles, not only for $k\gg l^{-1}$ (free motion), but also for $k\approx l^{-1}$ (diffusive motion).

E. Line fitting

For all wave numbers k, the dynamic structure factor $S(k,\omega)$ of the pure-He state [cf. Fig. 1(b)] can be described very well by three Lorentzians in ω: one central line and two side lines located at the frequencies $\pm\omega_s(k)$ [8]. The best three Lorentzian line fits are shown in Fig. 1(b) as solid curves. The locations of the side lines in $S(k,\omega)$ at $\omega_s(k)$ are given by solid arrows in this figure. Of the parameters obtained from the best fits, we only need here the frequency $\omega_s(k)$, which we shall call the extended sound dispersion of pure helium. We show $\omega_s(k)$ as a function of k in Fig. 7. One observes that $\omega_s(k)$ is close to the hydrodynamic sound dispersion $c_{He}k$, with $c_{He}=534$ m/s the speed of sound in the pure-He state [10].

We find for all k that the $S(k,\omega)$ of the He-Ne mixture cannot be described adequately with three Lorentzians. Instead, we need *four* Lorentzians for an accurate description of the total $S(k,\omega)$: two lines located at $\pm\omega_s^{(1)}(k)$, and two lines at $\pm\omega_s^{(2)}(k)$. In fact, we describe $S(k,\omega)$ of the He-Ne mixture by

$$S(k,\omega)=\frac{1}{\pi}S(k)\,\mathrm{Re}\sum_{j=1,2}\sum_{\mu=+,-}\frac{A_\mu^{(j)}(k)}{i\omega+z_\mu^{(j)}(k)} , \tag{3.8}$$

where the four Lorentzians are labeled with $j=1$ or 2 and $\mu=+$ or $-$ and where $A_+^{(j)}(k)=[A_-^{(j)}(k)]^*$ are complex-conjugate amplitudes and $z_+^{(j)}(k)=[z_-^{(j)}(k)]^*$ are complex conjugate frequencies. We define

$$z_\mu^{(j)}(k)=\mu\, i\omega_s^{(j)}(k)+z_s^{(j)}(k) , \tag{3.9}$$

with $\mu=+$ or $-$, and define $\omega_s^{(1)}(k)>\omega_s^{(2)}(k)$. Then for $j=1$ or 2, $z_s^{(j)}(k)$ is the half width and

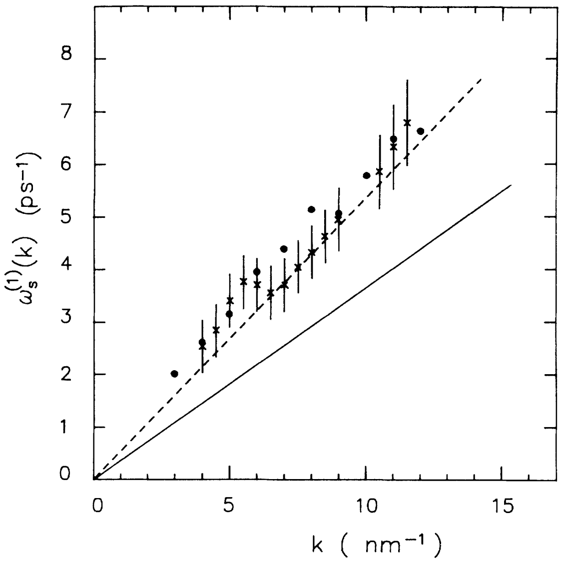

FIG. 7. Fast-sound frequency $\omega_s^{(1)}(k)$ as a function of k for $He_{0.65}Ne_{0.35}$ (crosses with error bars, read off from Figs. 1 and 2), the extended-sound frequency $\omega_s(k)$ for pure He (closed circles), and the hydrodynamic-sound dispersions ck for $He_{0.65}Ne_{0.35}$ (solid straight line, with $c=362$ m/s) and pure He (dashed straight line, with $c=534$ m/s).

$S(k)\mathrm{Re}A_{+}^{(j)}(k)=S(k)\mathrm{Re}A_{-}^{(j)}(k)$ is the area of the Lorentzian located at $\omega_s^{(j)}(k)$ or at $-\omega_s^{(j)}(k)$. The right-hand side of Eq. (3.8) contains eight free parameters that are all determined by a fit to the exponential $S(k,\omega)$. The best fits of $S(k,\omega)$ with four Lorentzians [cf. Eq. (3.8)] are shown in Figs. 1(a) and 2 as solid curves. For each k we also plot the locations $\omega_s^{(1)}(k)$ (solid arrow) and $\omega_s^{(2)}(k)$ (dashed arrow). One observes in Figs. 1(a) and 2 that the Lorentzian at $\omega_s^{(1)}(k)$ is located roughly where one sees a side peak or wing in $S(k,\omega)$, while no directly visible features are seen in $S(k,\omega)$ at $\omega_s^{(2)}(k)$. In Fig. 8 we plot the parameters of the four Lorentzians in Eq. (3.8) as functions of k. We show for $j=1$ or 2 $\omega_s^{(j)}(k)$ in Fig. 8(a), $z_s^{(j)}(k)$ in Fig. 8(b), $\mathrm{Re}A_{+}^{(j)}(k)$ in Fig. 8(c) and $\mathrm{Im}A_{+}^{(j)}(k)$ in Fig. 8(d). Due to the large number (eight) of free parameters in Eq. (3.8), the scatter in the results is considerable. Nevertheless, we can conclude the following. Since $\mathrm{Re}A_{+}^{(2)}(k)\gg\mathrm{Re}A_{+}^{(1)}(k)$ [cf. Fig. 8(c)], the area of the slow-sound line at $\omega_s^{(2)}(k)$ is much larger than the area of the fast-sound line at $\omega_s^{(1)}(k)$. Thus, slow sound dominates the shape of $S(k,\omega)$. Both the slow- and fast-sound lines are strongly asymmetric around $\omega_s^{(2)}(k)$ and $\omega_s^{(1)}(k)$, respectively, since both $\mathrm{Im}A_{+}^{(2)}(k)$ and $\mathrm{Im}A_{+}^{(1)}(k)$ are significantly different from zero [cf. Fig. 8(d)]. The two dominating Lorentzians at $\pm\omega_s^{(2)}(k)$ determine the central part of the total $S(k,\omega)$, in particular its half width $\omega_H(k)\approx z_s^{(2)}(k)$ [cf. Figs. 5 and 8(b)]. Therefore we refer to the two Lorentzians at $\pm\omega_s^{(2)}(k)$ as the "neon lines" that are not separately visible in $S(k,\omega)$, since $\omega_s^{(2)}(k)<z_s^{(2)}(k)$ [cf. Figs. 8(a) and 8(b)]. We refer to the two Lorentzians at $\pm\omega_s^{(1)}(k)$ as "helium lines," directly visible in $S(k,\omega)$ since they are well separated from the Ne lines $[\omega_s^{(1)}(k)>\omega_s^{(2)}(k)]$ and since $\omega_s^{(1)}(k)>z_s^{(1)}(k)$ (cf. Fig. 8). The fast-sound frequency $\omega_s^{(1)}(k)$ obtained from line fitting [cf. Fig. 8(a)] agrees very well with the location of the visible side peak directly read off from $S(k,\omega)$, which is plotted as a function of k in Fig. 7. One also sees in Fig. 7 that the location $\omega_s^{(1)}(k)$ of the He lines in $S(k,\omega)$ of the He-Ne mixture is virtually indistinguishable from the extended sound dispersion $\omega_s(k)$ of the pure-He state. In addition, one observes in Fig. 7 that $\omega_s^{(1)}(k)$ is significantly larger than the hydrodynamic sound dispersion ck of the He-Ne mixture. Here $c=362$ m/s is the speed of sound of the He-Ne mixture, calculated from a phenomenological equation of state [17,18]. The sudden drop in $\omega_s^{(1)}(k)$ seen in Fig. 8(a) at $k=13$ nm^{-1} is probably not significant, as will be discussed at the end of Sec. IV D.

IV. KINETIC MODEL

In this section we present a kinetic model that is consistent with the experimentally observed total dynamic

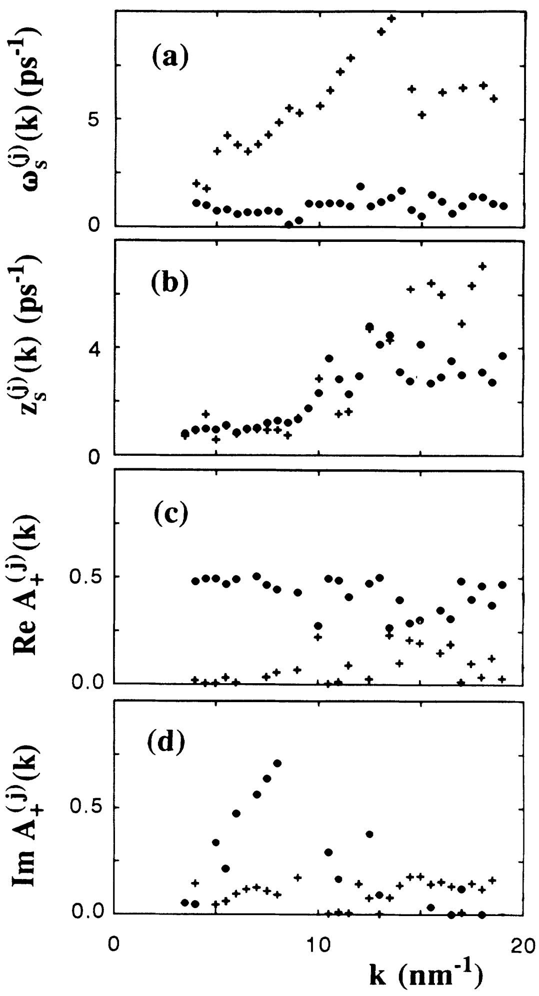

FIG. 8. The eight parameters of the four Lorentzians that describe $S(k,\omega)$ of $He_{0.65}Ne_{0.35}$ [cf. Eq. (3.8)] as functons of k. These are (a) $\omega_s^{(j)}(k)$, (b) $z_s^{(j)}(k)$, (c) Re $A_{+}^{(j)}(k)$, and (d) Im $A_{+}^{(j)}(k)$. Crosses refer to $j=1$ (fast sound) and dots to $j=2$ (slow sound).

structure factor $S(k,\omega)$ [cf. Eq. (2.1)] for $k>k_H$, with the phenomenological description of $S(k,\omega)$ in terms of four Lorentzians discussed in Sec. III, and which can be extended to the hydrodynamic region $k<k_H$. The kinetic model is based on five microscopic variables. This set includes both the four hydrodynamic variables and the four microscopic variables discussed in Ref. [3], which proved useful to understand the dynamics in a MD Li-Pb mixture. To apply this model to the present He-Ne mixture, we need the partial static structure factors $S_{11}(k)$, $S_{22}(k)$, and $S_{12}(k)$. We discuss an approximation for these $S_{jl}(k)$ in Sec. IV A, and we present the five microscopic values in Sec. IV B, the kinetic model in Sec. IV C, the results of model fitting in Sec. IV D, and the transition to hydrodynamics in Sec. IV E.

A. Static structure factors

The partial static structure factors $S_{jl}(k)$ are defined by Eqs. (2.4) and (2.5), i.e.,

$$S_{jl}(k)=F_{jl}(k,0)\ , \tag{4.1}$$

with j or $l=1,2$. The total static structure factor $S_T(k)$ of the mixture (irrespective of the scattering lengths) is defined by

$$S_T(k)=x_1S_{11}(k)+x_2S_{22}(k)+2(x_1x_2)^{1/2}S_{12}(k)\ . \tag{4.2}$$

We use the following three (approximate) relations:

$$\begin{aligned} S_{11}(k)&=1+x_1[S_T(k)-1]\ ,\\ S_{22}(k)&=1+x_2[S_T(k)-1]\ ,\\ S_{12}(k)&=(x_1x_2)^{1/2}[S_T(k)-1]\ . \end{aligned} \tag{4.3}$$

These so-called ideal mixing rules are valid exactly for binary mixtures of particles with different masses (m_2/m_1 arbitrary) but interparticle potentials that do not depend on the species (in particular for hard-sphere mixtures with $\sigma_2/\sigma_1=1$). In that case, $S_T(k)$ of Eq. (4.2) is the static structure factor of the corresponding pure fluid in which all particles are made identical by setting $m_2/m_1=1$. For the hard-sphere mixture ($\sigma_2/\sigma_1=1.16$) corresponding to our present He-Ne fluid, we find from the Percus-Yevick theory that Eq. (4.3) holds well, i.e., within 5% for all k. We assume that Eq. (4.3) may be applied also to our present He-Ne mixture (within about the same accuracy). Thus, using Eqs. (3.2), (4.2), and (4.3), one has (approximately)

$$S_T(k)=1+(x_1b_1^*+x_2b_2^*)^{-2}[S(k)-1]\ , \tag{4.4}$$

so that $S_T(k)$ is expressed directly in terms of the experimentally observed total static structure factor $S(k)$. Since $(x_1b_1^*+x_2b_2^*)^{-2}=1.028$ is close to 1, $S_T(k)$ is virtually indistinguishable from $S(k)$, as given in Fig. 3(b). We obtain the partial static structure factors $S_{jl}(k)$ of our He-Ne mixture from the experimental $S(k)$ and Eqs. (4.4) and (4.3).

B. Basic variables

We consider the following five basic $\mathbf{k}$-dependent microscopic variables of the He-Ne mixture. First, the microscopic density of He particles $\delta n_1(\mathbf{k})=\delta n_1(\mathbf{k},0)$ [given by Eq. (2.5) with $t=0$] and the microscopic density of Ne particles $\delta n_2(\mathbf{k})=\delta n_2(\mathbf{k},0)$ [cf. Eq. (2.5)]. Next, the two corresponding microscopic longitudinal velocities ($l=1$ or 2)

$$\delta u_l(\mathbf{k})=\frac{1}{\sqrt{N_l}}\sum_{p=1}^{N_l}(\mathbf{v}_l^{(p)}\cdot\mathbf{k}/k)e^{i\mathbf{k}\cdot\mathbf{r}_l^{(p)}}\ , \tag{4.5}$$

with $l=1$ for He and $l=2$ for Ne. Here $\mathbf{r}_l^{(p)}$ and $\mathbf{v}_l^{(p)}$ are the location and velocity at time $t=0$ of particle p of species l, respectively. Finally, the total microscopic energy density of the mixture, defined by

$$\delta e(\mathbf{k})=\frac{1}{\sqrt{N_1+N_2}}\sum_{l=1}^{2}\sum_{p=1}^{N_l}\varepsilon_l^{(p)}e^{i\mathbf{k}\cdot\mathbf{r}_l^{(p)}}\ , \tag{4.6}$$

with $\varepsilon_l^{(p)}$ the total (kinetic and potential) energy of particle p of species l,

$$\varepsilon_l^{(p)}=\tfrac{1}{2}m_l\mathbf{v}_l^{(p)2}+\tfrac{1}{2}\sum_{j=1}^{2}\sum_{q=1}^{N_j}\phi_{jl}(|\mathbf{r}_j^{(q)}-\mathbf{r}_l^{(p)}|)\ , \tag{4.7}$$

where $\phi_{jl}(r)$ is the interaction potential between a particle of species j and a particle of species l at distance r.

We need the fluctuation formulas (j or $l=1,2$)

$$\begin{aligned} &\langle[\delta n_j(\mathbf{k})]^*\delta n_l(\mathbf{k})\rangle=S_{jl}(k)\ ,\\ &\langle[\delta u_j(\mathbf{k})]^*\delta u_l(\mathbf{k})\rangle=\delta_{jl}(\beta m_j)^{-1}\ ,\\ &\langle[\delta n_j(\mathbf{k})]^*\delta u_l(\mathbf{k})\rangle=\langle[\delta e(\mathbf{k})]^*\delta u_l(\mathbf{k})\rangle=0\ , \end{aligned} \tag{4.8}$$

which follow from Eqs. (2.5), (4.1), and (4.5)–(4.7). By taking linear combinations and using Eq. (4.8), we construct five equivalent basic variables $\delta a_j(\mathbf{k})$ of the mixture that are orthonormal, i.e., satisfy

$$\langle[\delta a_j(\mathbf{k})]^*\delta a_l(\mathbf{k})\rangle=\delta_{jl}\ , \tag{4.9}$$

with j or $l=c,N,P,T,v$. These five labels refer to fluctuations in the mutual number concentration (c), the total number density (N), the total momentum (P), the total temperature (T), and the mutual relative velocity of the constituents (v). The five basic fluctuations $\delta a_j(\mathbf{k})$ of the fluid are schematically represented in Fig. 9 by five circles labeled c, N, P, T, and v. The microscopic concentration is given by

$$\delta a_c(\mathbf{k})=\frac{1}{A_c(k)}[x_2^{1/2}\delta n_1(\mathbf{k})-x_1^{1/2}\delta n_2(\mathbf{k})]\ , \tag{4.10}$$

with the normalization factor

$$\begin{aligned} A_c(k)=[&x_1S_{22}(k)+x_2S_{11}(k)\\ &-2(x_1x_2)^{1/2}S_{12}(k)]^{1/2}\ . \end{aligned} \tag{4.11}$$

The microscopic total number density is

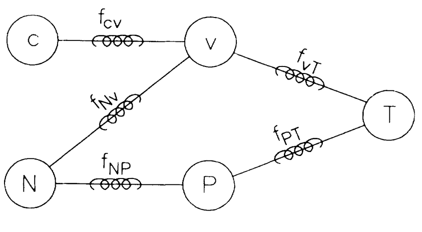

FIG. 9. Schematic representation of the 5×5 kinetic model matrix $H(k)$ of Eq. (4.22). The circles represent the five basic variables c, N, P, T, and v, and the springs represent the five nonvanishing elastic corces $f_{jl}(k)$ of $H(k)$.

$$\delta a_N(\mathbf{k})=\frac{1}{A_N(k)}\{[x_1^{1/2}S_{22}(k)-x_2^{1/2}S_{12}(k)]\delta n_1(\mathbf{k}) +[x_2^{1/2}S_{11}(k)-x_1^{1/2}S_{12}(k)] \times\delta n_2(\mathbf{k})\}\ , \tag{4.12}$$

with

$$A_N(k)=A_c(k)\{S_{11}(k)S_{22}(k)-[S_{12}(k)]^2\}^{1/2}\ . \tag{4.13}$$

The microscopic total momentum is

$$\delta a_P(\mathbf{k})=(\beta/\overline{m})^{1/2}[x_1^{1/2}m_1\delta u_1(\mathbf{k})+x_2^{1/2}m_2\delta u_2(\mathbf{k})]\ , \tag{4.14}$$

with $\overline{m}=x_1m_1+x_2m_2$ the averaged mass of a particle. The microscopic temperature is

$$\delta a_T(\mathbf{k})=\frac{1}{A_T(k)}\{\delta e(\mathbf{k})-\langle\delta e(\mathbf{k})[\delta a_c(\mathbf{k})]^*\rangle\delta a_c(\mathbf{k}) -\langle\delta e(\mathbf{k})[\delta a_N(\mathbf{k})]^*\rangle\delta a_N(\mathbf{k})\}\ , \tag{4.15}$$

where the normalization factor $A_T(k)$ follows from Eq. (4.9) with $j=l=T$, but will not be explicitly needed here. Finally, the microscopic relative velocity is

$$\delta a_v(\mathbf{k})=(\beta m_1m_2/\overline{m})^{1/2}[x_2^{1/2}\delta u_1(\mathbf{k})-x_1^{1/2}\delta u_2(\mathbf{k})]\ . \tag{4.16}$$

One readily verifies from Eq. (4.8) that the five variables $\delta a_j(\mathbf{k})$ satisfy Eq. (4.9) for all $j=c,N,P,T,v$. We will express the microscopic densities $\delta n_1(\mathbf{k})$ and $\delta n_2(\mathbf{k})$ in terms of $\delta a_c(\mathbf{k})$ and $\delta a_N(\mathbf{k})$ using

$$\delta n_j(\mathbf{k})=\sum_{l=c,N}s_l^{(j)}(k)\delta a_l(\mathbf{k})\ , \tag{4.17}$$

where $j=1$ or 2 and

$$\begin{aligned} s_c^{(1)}(k)&=\frac{1}{A_c(k)}[x_2^{1/2}S_{11}(k)-x_1^{1/2}S_{12}(k)]\ ,\\ s_N^{(1)}(k)&=x_1^{1/2}A_N(k)/A_c(k)^2\ ,\\ s_c^{(2)}(k)&=\frac{1}{A_c(k)}[x_2^{1/2}S_{12}(k)-x_1^{1/2}S_{22}(k)]\ ,\\ s_N^{(2)}(k)&=x_2^{1/2}A_N(k)/A_c(k)^2\ . \end{aligned} \tag{4.18}$$

We use these transformation formulas to express the density time correlation functions $F_{jl}(k,t)$ of Eq. (2.4) in terms of time correlation functions of the orthonormal set $\delta a_j(\mathbf{k})$. We remark that the four $\delta a_j(\mathbf{k})$ with $j=c,N,P,T$ are the hydrodynamic variables, and the four $\delta a_j(\mathbf{k})$ with $j=c,N,P,v$ are those used in Refs. [1–3].

C. Kinetic matrix

We introduce the 25 time correlation functions $G_{jl}(k,t)$ between the five basic orthonormal variables $\delta a_j(\mathbf{k})$ by

$$G_{jl}(k,t)=\langle[\delta a_j(\mathbf{k})]^*e^{tL}\delta a_l(\mathbf{k})\rangle\ , \tag{4.19}$$

with j or $l=c,N,P,T,v$, with L the Liouville operator of the mixture (given in the Appendix), and $\exp(tL)$ the corresponding streaming operator replacing all positions and velocities of the particles at time $t=0$ by those at time t. Then the intermediate partial scattering functions $F_{jl}(k,t)$ of Eq. (2.4) are given by [cf. Eq. (4.17)]

$$F_{jl}(k,t)=\sum_{p=c,N}\sum_{q=c,N}s_p^{(j)}(k)s_q^{(l)}(k)G_{pq}(k,t)\ , \tag{4.20}$$

with j or $l=1,2$ and $s_p^{(j)}(k)$ with $p=c$ or N given by Eq. (4.18). In our kinetic model we replace for $t\geq 0$ the Liouville operator L in Eq. (4.19) by $-H(k)$, where $H(k)$ is a 5×5 matrix that effectively (and approximately) describes the dynamics of the five basic microscopic variables $\delta a_j(\mathbf{k})$. Thus, for j or $l=c,N,P,T,v$ and $t\geq 0$,

$$G_{jl}(k,t)=[e^{-tH(k)}]_{jl}\ , \tag{4.21}$$

where the symmetric kinetic matrix $H(k)$ is given by (cf. the Appendix)

$$H(k)=\begin{bmatrix} 0 & 0 & 0 & 0 & if_{cv}(k)\\ 0 & 0 & if_{NP}(k) & 0 & if_{Nv}(k)\\ 0 & if_{NP}(k) & z_{PP}(k) & if_{PT}(k) & 0\\ 0 & 0 & if_{PT}(k) & z_{TT}(k) & if_{Tv}(k)\\ if_{cv}(k) & if_{Nv}(k) & 0 & if_{Tv}k & z_{vv}(k) \end{bmatrix}\ , \tag{4.22}$$

where

$$
\begin{aligned}
f_{cv}(k)&=\frac{k}{(\beta\bar{m})^{1/2}}\frac{1}{A_c(k)}\left[\frac{\bar{m}^2}{m_1m_2}\right]^{1/2},\\
f_{NP}(k)&=\frac{k}{(\beta\bar{m})^{1/2}}\frac{A_c(k)^2}{A_N(k)},\\
f_{Nv}(k)&=\frac{k}{(\beta\bar{m})^{1/2}}\frac{1}{A_N(k)}\{(x_1x_2m_2/m_1)^{1/2}S_{22}(k)-(x_1x_2m_1/m_2)^{1/2}S_{11}(k)\\
&\qquad+[x_1(m_1/m_2)^{1/2}-x_2(m_2/m_1)^{1/2}]S_{12}(k)\}\ .
\end{aligned}
\tag{4.23}
$$

Explicit expressions for the remaining so-called "forces" $f_{jl}(k)$ in $H(k)$ and for the damping rates $z_{jj}(k)$ are given in the Appendix. The five nonvanishing elastic forces $f_{jl}(k)$ of $H(k)$ are schematically represented in Ref. 9 by springs between the basic variables j or $l=c,N,P,T,v$. By definition of the microscopic concentration fluctuation $\delta a_c(\mathbf{k})$ [cf. Eq. (4.10) and the Appendix], there is no elastic force between c and P (cf. Fig. 9). This implies that a fluctuation in the microscopic concentration c does not directly induce a variation in the total microscopic momentum P.

We need the spectrum $S_{cc}(k,\omega)$ of concentration fluctuations, the spectrum $S_{NN}(k,\omega)$ of total number fluctuations, and the cross spectrum $S_{cN}(k,\omega)$, defined by (α or $\beta=c,N$)

$$
\begin{aligned}
S_{\alpha\beta}(k,\omega)&=\frac{1}{2\pi}\int_{-\infty}^{+\infty}dt\, e^{-i\omega t}G_{\alpha\beta}(k,t)\\
&=\frac{1}{\pi}\mathrm{Re}\int_0^{\infty}dt\, e^{-i\omega t}G_{\alpha\beta}(k,t)\ ,
\end{aligned}
\tag{4.24}
$$

where we have used the fact that the $G_{\alpha\beta}(k,t)$ are symmetric in t [cf. Eq. (4.19)]. Thus, from Eq. (4.21),

$$
S_{\alpha\beta}(k,\omega)=\frac{1}{\pi}\mathrm{Re}\left[\frac{1}{i\omega+H(k)}\right]_{\alpha\beta},
\tag{4.25}
$$

with α or $\beta=c,N$.

D. Model fitting

Throughout this section we use the ideal mixing rules given by Eq. (4.3). Then $A_c(k)$ [cf. Eq. (4.11)] and $A_N(k)$ [cf. Eq. (4.23)] are

$$
\begin{aligned}
A_c(k)&=1\ ,\\
A_N(k)&=[S_T(k)]^{1/2}\ ,
\end{aligned}
\tag{4.26}
$$

with $S_T(k)$ defined by Eq. (4.2). The transformation parameters $s_l^{(j)}(k)$ of Eq. (4.17) are then given by

$$
\begin{aligned}
s_c^{(1)}(k)&=(x_2)^{1/2}\ ,\\
s_N^{(1)}(k)&=[x_1S_T(k)]^{1/2}\ ,\\
s_c^{(2)}(k)&=-(x_1)^{1/2}\ ,\\
s_N^{(2)}(k)&=[x_2S_T(k)]^{1/2}\ ,
\end{aligned}
\tag{4.27}
$$

and the three forces $f_{cv}(k)$, $f_{NP}(k)$, and $f_{Nv}(k)$ of $H(k)$ in Eq. (4.23) are

$$
\begin{aligned}
f_{cv}(k)&=\frac{k}{(\beta\bar{m})^{1/2}}\left[\frac{\bar{m}^2}{m_1m_2}\right]^{1/2},\\
f_{NP}(k)&=\frac{k}{(\beta\bar{m})^{1/2}}\frac{1}{\sqrt{S_T(k)}}\ ,\\
f_{Nv}(k)&=\frac{k}{(\beta\bar{m})^{1/2}}\frac{1}{\sqrt{S_T(k)}}(x_1x_2)^{1/2}\frac{m_2-m_1}{(m_1m_2)^{1/2}}\ .
\end{aligned}
\tag{4.28}
$$

Thus the force $f_{cv}(k)=v_{cv}k$ is linear in k for all k with velocity $v_{cv}=198$ m/s [using that $(\beta\bar{m})^{-1/2}=184$ m/s]. The forces $f_{NP}(k)$ and $f_{Nv}(k)$ are proportional, i.e., $f_{Nv}(k)=0.86f_{NP}(k)$, and behave linearly in k for small k, i.e., for $0\leq k<8$ nm^{-1}, where $S_T(k)=0.38$ is constant (cf. Fig. 3). Thus for $k\to 0$, $f_{NP}(k)=v_{NP}k$ and $f_{Nv}(k)=v_{Nv}k$, with velocities $v_{NP}=300$ m/s and $v_{Nv}=260$ m/s.

We write the experimentally observed $S(k,\omega)$ of Eq. (2.1) in terms of the spectra $S_{cc}(k,\omega)$ $S_{NN}(k,\omega)$, and $S_{cN}(k,\omega)$ defined by Eqs. (4.24) and (4.19) using Eqs. (2.3), (4.20), and (4.27), so that

$$
\begin{aligned}
S(k,\omega)&=C_{cc}(k)S_{cc}(k,\omega)+C_{NN}(k)S_{NN}(k,\omega)\\
&\quad+C_{cN}(k)S_{cN}(k,\omega)\ ,
\end{aligned}
\tag{4.29}
$$

with

$$
\begin{aligned}
C_{cc}(k)&=x_1x_2(b_1^*-b_2^*)^2\ ,\\
C_{NN}(k)&=(x_1b_1^*+x_2b_2^*)^2S_T(k)\ ,\\
C_{cN}(k)&=2(x_1x_2)^{1/2}(b_1^*-b_2^*)\\
&\quad\times(x_1b_1^*+x_2b_2^*)[S_T(k)]^{1/2}\ .
\end{aligned}
\tag{4.30}
$$

Thus $S(k,\omega)$ is strongly dominated by $S_{NN}(k,\omega)$, since $C_{NN}(k)=0.973S_T(k)$ is of order 1, $C_{cc}(k)=0.027$ is very small, and $C_{cN}(k)=-0.322[S_T(k)]^{1/2}$ is intermediate, and since the $S_{\alpha\beta}(k,\omega)$ are normalized; i.e., $\int_{-\infty}^{+\infty}d\omega\, S_{\alpha\beta}(k,\omega)=\delta_{\alpha\beta}$, with α or $\beta=c,N$ [cf. Eqs. (4.9), (4.19), and (4.24)].

We describe our experimental $S(k,\omega)$ in terms of $S_{\alpha\beta}(k,\omega)$ (α or $\beta=c,N$), cf. Eq. (4.29), with $S_{\alpha\beta}(k,\omega)$ given by Eq. (4.25), in which the matrix $H(k)$ is given by Eq. (4.22). For $f_{cv}(k)$, $f_{NP}(k)$, and $f_{Nv}(k)$ in $H(k)$, we use Eq. (4.28), with $S_T(k)$ obtained from the experimental $S(k)$, cf. Eq. (4.4). We fit $S(k,\omega)$ with the five unknown elements of the matrix $H(k)$: $f_{PT}(k)$, $f_{Tv}(k)$ and $z_{PP}(k)$, $z_{TT}(k)$, and $z_{vv}(k)$ as fit parameters. We find that the fits are as good as the fits with four Lorentzians shown in Figs. 1(a) and 2. We show the resulting elements of the matrix $H(k)$ in Fig. 10.

The kinetic matrix $H(k)$ so obtained from the experimental $S(k,\omega)$ has five eigenmodes (i.e., eigenvalues and corresponding eigenvectors) that we call the effective eigenmodes of the He-Ne mixture, since they effectively describe the dynamics of the five basic variables $\delta a_j(\mathbf{k})$ with $j=c,N,P,T,v$. These five effective eigenmodes of $H(k)$ lead directly to a description in terms of five Lorentzians in ω for $S_{\alpha\beta}(k,\omega)$ with α or $\beta=c,N$ [cf. Eq. (4.25)], as well as for the partial dynamic structure factors $S_{jl}(k,\omega)$ with j or $l=1,2$ and the total experimental dynamic structure factor $S(k,\omega)$ [cf. Eq. (4.29)]. We plot the five eigenvalues of $H(k)$ in Fig. 11.

The matrix $H(k)$ has one diffusive-type eigenmode, i.e., one *real* eigenvalue $z_c(k)$:

$$H(k)\psi_c(k)=z_c(k)\psi_c(k)\ , \tag{4.31}$$

with corresponding eigenvector $\psi_c(k)$, which has its main component on the microscopic concentration (c). Thus the resulting central Lorentzian with half width $z_c(k)$ shows up strongly in $S_{cc}(k,\omega)$ and very weakly in $S_{NN}(k,\omega)$ and $S_{cN}(k,\omega)$. We find, in fact, that this central Lorentzian does not show up significantly in the experimental $S(k,\omega)$ [cf. Eq. (4.29)].

The matrix $H(k)$ has four propagating eigenmodes, given by

$$H(k)\psi_\mu^{(j)}(k)=z_\mu^{(j)}(k)\psi_\mu^{(j)}(k)\ , \tag{4.32}$$

labeled with $j=1$ or 2 and $\mu=+$ or $-$, where

$$z_\mu^{(j)}(k)=\mu i\,\omega_s^{(j)}(k)+z_s^{(j)}(k) \tag{4.33}$$

are two pairs of complex conjugate eigenvalues and $\psi_\mu^{(j)}(k)$ are two pairs of corresponding complex-conjugate eigenvectors $\psi_+^{(j)}(k)=[\psi_-^{(j)}(k)]^*$. The four propagating eigenmodes of $H(k)$ show up strongly in $S_{NN}(k,\omega)$ and almost completely determine the experimental dynamic structure factor $S(k,\omega)$, which is therefore, in practice, a sum of four Lorentzians only. Indeed, the eigenvalues $z_\mu^{(j)}(k)$ obtained from $H(k)$, cf. Eq. (4.32) and Fig. 11, are virtually indistinguishable from the $z_\mu^{(j)}(k)$ obtained from the four-Lorentzian description, cf. Eq. (3.8) and Fig. 8. One also observes in Figs. 8 and 11 that the scatter in the $z_\mu^{(j)}(k)$ derived from $H(k)$ via a *five*-parameter fit (Fig. 11) is less than the scatter in the $z_\mu^{(j)}(k)$ derived from four Lorentzians via an *eight*-parameter fit (Fig. 8). In particular, the k dependence of the fast-sound frequency $\omega_s^{(1)}(k)$ in Fig. 11(a) is smoother than that of $\omega_s^{(1)}(k)$ in Fig. 8(a). Therefore, the sudden drop in $\omega_s^{(1)}(k)$ seen in Fig. 8(a) at $k=13\ \mathrm{nm}^{-1}$ is possibly not significant, since it is absent in Fig. 11(a).

E. Hydrodynamics

In this section we extrapolate the kinetic matrix $H(k)$ given by Eq. (4.22) and obtained from the experimental $S(k,\omega)$ for $4\le k\le 25\ \mathrm{nm}^{-1}$ to the hydrodynamic regime, i.e., to $k\rightarrow 0$. As discussed in the Appendix, all five independent forces $f_{jl}(k)$ in $H(k)$ behave linearly in k for $k\rightarrow 0$, i.e.,

$$f_{jl}(k)=v_{jl}k\ , \tag{4.34}$$

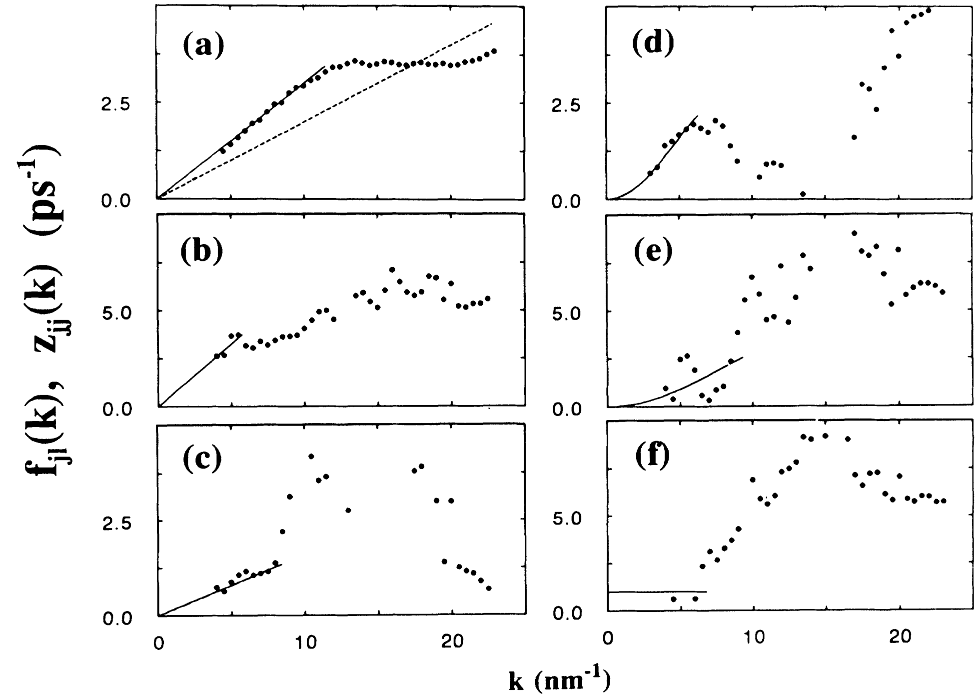

FIG. 10. Elements $f_{jl}(k)$ and $z_{jj}(k)$ of the matrix $H(k)$ [cf. Eq. (4.22)] as functions of k. The dots refer to (a) $f_{NP}(k)$, (b) $f_{Tv}(k)$, (c) $f_{PT}(k)$, (d) $z_{PP}(k)$, (e) $z_{TT}(k)$, and (f) $z_{vv}(k)$. Solid curves are the corresponding continuous extensions to $k=0$. The dashed straight line in (a) is $f_{cv}(k)$. $f_{Nv}(k)=0.86f_{NP}(k)$ is not shown.

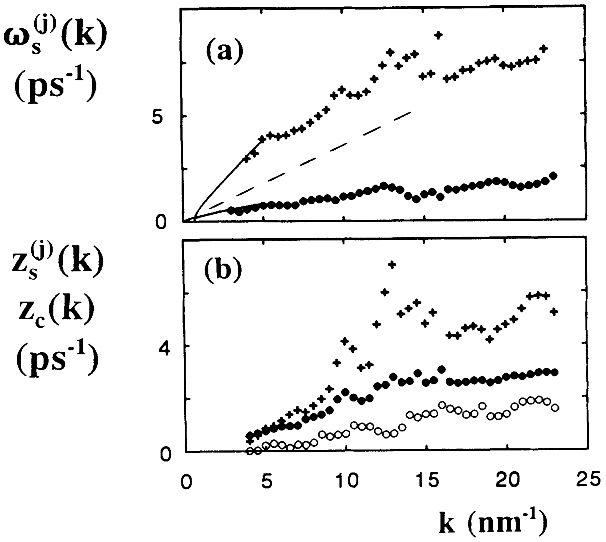

FIG. 11. The five eigenvalues of $H(k)$ as functions of k [cf. Eqs. (4.31)–(4.33)]. Crosses (fast sound) refer to (a) $\omega_s^{(1)}(k)$ and (b) $z_s^{(1)}(k)$. Closed circles (slow sound) refer to (a) $\omega_s^{(2)}(k)$ and (b) $z_s^{(2)}(k)$. Open circles in (b) refer to $z_c(k)$. The dashed straight line in (a) is ck, with $c=362$ m/s. Solid curves in (a) are the extensions $\omega_s^{(j)}(k)$ to $k=0$ of Fig. 12.

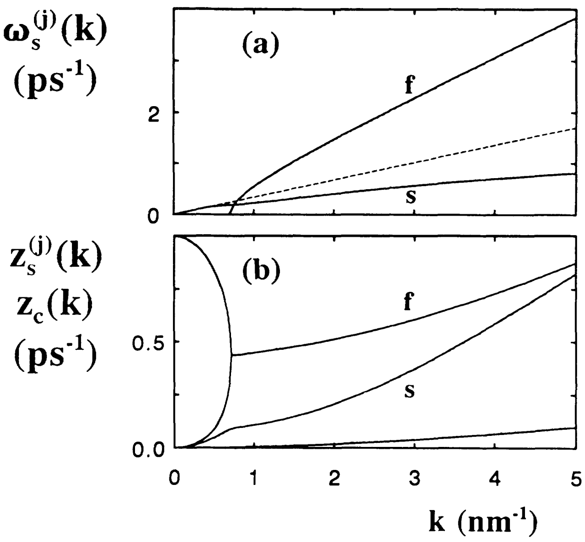

FIG. 12. The five eigenvalues of $H(k)$ as functions of k extended to $k=0$ (from the solid curves in Fig. 10). Solid curves labeled f (fast sound) refer to (a) $\omega_s^{(1)}(k)$ and (b) $z_s^{(1)}(k)$. Solid curves labeled s (slow sound) refer to (a) $\omega_s^{(2)}(k)$ and (b) $z_s^{(2)}(k)$. The unlabeled curve in (b) is $z_c(k)$. The dashed straight line in (a) is ck, with $c=362$ m/s.

with j or $l=c,N,P,T,v$, and where the three velocities v_{cv}, v_{NP}, and v_{Nv} are given below Eq. (4.28), leaving the two velocities v_{PT} and v_{Tv} as unknown quantities. Furthermore (cf. the Appendix), the two hydrodynamic damping rates $z_{PP}(k)$ and $z_{TT}(k)$ in $H(k)$ vanish quadratically in k when $k\rightarrow 0$, while the nonhydrodynamic (i.e., kinetic) damping rate $z_{vv}(k)$ approaches a constant $z_{vv}(0)$ then. We fit all our $S(k,\omega)$ data with $k\leq 6$ nm^{-1} simultaneously to $H(k)$ [cf. Eqs. (4.29) and (4.25)], with $f_{jl}(k)$ replaced by $v_{jl}(k)$ [cf. Eq. (4.34)], $z_{vv}(k)$ replaced by $z_{vv}(0)$, and $z_{jj}(k)$ replaced by

$$z_{jj}(k)=\phi_j k^2+B_j k^4\ , \tag{4.35}$$

with $j=P$ or T.

We find that the resulting best approximations to $S(k,\omega)$ in this seven-parameter fit are good, with $v_{PT}=160$ m/s, $v_{Tv}=650$ m/s, $z_{vv}(0)=1.0$ ps^{-1}, $\phi_P=7.8\times10^{-2}$ nm^2/ps, $B_p=-5.8\times10^{-4}$ nm^4/ps, $\phi_T=3.9\times10^{-2}$ nm^2/ps, and $B_T=-1.1\times10^{-4}$ nm^4/ps. These (rough) extensions for the elements of the matrix $H(k)$ to $k\rightarrow 0$ are shown in Fig. 10 as solid curves. Thus, we can also (roughly) extend the eigenmodes of $H(k)$ to the hydrodynamic regime $0\leq k<k_H$. In Figs. 11 and 12 we show the extensions of the five eigenvalues $z_c(k)$ [cf. Eq. (4.31)] and $z_\mu^{(j)}(k)=\mu i\omega_s^{(j)}(k)+z_s^{(j)}(k)$, with $j=1$ or 2 and $\mu=+$ or $-$ [cf. Eq. (4.33)] of $H(k)$ to $k\rightarrow 0$, where we find that $k_H=0.7$ nm^{-1}. One sees in Figs. 11 and 12 that $z_c(k)$ extends smoothly to $0\leq k<k_H$, where $z_c(k)=D_c k^2$, with $D_c=0.005$ nm^2/ps, the concentration diffusion coefficient. In Fig. 12 one sees that the slow-sound mode eigenfrequency $\omega_s^{(2)}(k)$ becomes linear, $\omega_s^{(2)}(k)=ck$ for $0\leq k<k_H$. Here $c=(v_{NP}^2+v_{PT}^2)^{1/2}$ is the hydrodynamic sound velocity of the mixture determined by the (hydrodynamic) velocities v_{NP} and v_{PT}, which are both obtained from our present neutron-scattering experiment at $k>k_H$. This value of $c=340$ m/s is not too different from the estimate $c=362$ m/s derived from the phenomenological equation of state. For $0\leq k<k_H$, the corresponding damping $z_s^{(2)}(k)$ becomes quadratic in k, i.e., $z_s^{(2)}(k)=\Gamma k^2$, with $\Gamma=0.19$ nm^2/ps the sound damping coefficient (cf. Fig. 12). The fast-sound mode frequency $\omega_s^{(1)}(k)$ vanishes for $0\leq k<k_H$, and the damping $z_s^{(1)}(k)$ ~~splits into two branches (cf. Figs. 11 and 12). One~~ branch approaches the constant $z_{vv}(0)=1.0$ ps^{-1} and corresponds to a kinetic mode of $H(k)$ [eigenvector $\sim\delta a_v(\mathbf{k})$]. The other branch of $z_s^{(1)}(k)$ tends to zero quadratically in k, i.e., $z_s^{(1)}(k)=ak^2$, with $a=0.27$ nm^2/ps the heat diffusivity. Thus, in hydrodynamics $(0\leq k<k_H)$, $S(k,\omega)$ is a sum of four Lorentzians: two central lines with half widths $D_c k^2$ and ak^2, and two lines located at $\pm ck$ and half widths Γk^2. In hydrodynamics, the kinetic eigenmode of $H(k)$ does not show up in $S(k,\omega)$, since $\delta a_v(\mathbf{k})$ is orthogonal to the microscopic number densities $\delta n_1(\mathbf{k})$ and $\delta n_2(\mathbf{k})$ so that corresponding amplitudes in $S(k,\omega)$ vanish.

V. DISCUSSION

The experimentally observed total dynamic structure factor $S(k,\omega)$ [cf. Eq. (2.1)] of our mixture $\mathrm{He}_{0.65}\mathrm{Ne}_{0.35}$ at 39.3 K and 114 bar can be represented very well by four Lorentzian lines [cf. Figs. 1(a) and 2]. Two directly visible lines are located at $\pm\omega_s^{(1)}(k)$, with $\omega_s^{(1)}(k)>ck$ (fast sound) and two not separately visible lines at $\pm\omega_s^{(2)}(k)$, with $\omega_s^{(2)}(k)<ck$ (slow sound), where $c=362$ m/s is the intermediate hydrodynamic sound velocity of the mixture.

We attribute the fast-sound lines at $\pm\omega_s^{(1)}(k)$ to fast oscillations of the light helium (1) particles, since $S(k,\omega)$ is in its wings dominated by the helium contribution $S_{11}(k,\omega)$ in Eq. (2.1). This follows from the behavior of the zeroth- [$S(k)$; cf. Fig. 3] and second- [$M_2(k)$; cf. Fig. 4] frequency moments of the total $S(k,\omega)$. In addition, $\omega_s^{(1)}(k)$ of the He-Ne mixture is virtually indistinguishable from the (extended) sound dispersion $\omega_s(k)$ observed for corresponding pure helium (cf. Fig. 7).

We attribute the slow-sound lines at $\pm\omega_s^{(2)}(k)$ in $S(k,\omega)$ of the He-Ne mixture to slow oscillations of the heavy neon (2) particles. The reason is that the two lines at $\pm\omega_s^{(2)}(k)$ (merged into one another) determine the central part of $S(k,\omega)$, while this central part is determined mainly by the motion of the Ne particles. This follows from the behavior of $S(k)$, $M_2(k)$, and the half width $\omega_H(k)$ of $S(k,\omega)$, as shown in Figs. 5 and 6.

The four Lorentzians of $S(k,\omega)$ can be described by a kinetic model that involves the 5×5 model matrix $H(k)$ of Eq. (4.22). This matrix $H(k)$ approximately determines the dynamics of the five basic microscopic variables labeled c, N, P, T, and v [see Fig. 9 and Eq. (4.9)]. The forces $f_{jl}(k)$ of $H(k)$ are schematically represented in Fig. 9 as springs between the basic variables j and l. We see in Fig. 10 that the force $f_{vT}(k)$ between v and T is the largest of the five forces in $H(k)$. In fact, it strongly determines the two fast-sound eigenmodes of $H(k)$, i.e., $\omega_s^{(1)}(k)\approx f_{vT}(k)$. The smaller force $f_{PT}(k)$ between P and T is most relevant for the two slow-sound eigenmodes of $H(k)$, i.e., $\omega_s^{(2)}(k)\approx f_{PT}(k)$, at least for smaller-$k$ values (cf. Figs. 10 and 11).

In hydrodynamics, for small $k<k_H=0.7\ \mathrm{nm}^{-1}$, all five forces $f_{jl}(k)\sim k$ vanish proportional to k, the two hydrodynamic transport coefficients $z_{PP}(k)\sim z_{TT}(k)\sim k^2$ vanish proportional to k^2, while the kinetic transport coefficient $z_{vv}(k)\approx z_{vv}(0)$ approaches a constant. It is as if the kinetic variable v in Fig. 9 becomes a "massive object" for $k\rightarrow 0$, which cannot oscillate. Indeed, normal-sound oscillations arise for $k\rightarrow 0$ between the variables N, P, and T, with the hydrodynamic sound velocity determined by the forces $f_{NP}(k)$ and $f_{PT}(k)$ alone (see Sec. IV E). Thus, quite naturally, the slow-sound modes of $H(k)$ observed for $k>k_H$ merge into hydrodynamic sound for $k<k_H$ and fast sound vanishes (cf. Figs. 11 and 12), since fast sound involves the kinetic variable v and slow sound mainly involves the hydrodynamic variables P and T. It would be interesting to see whether neutron-scattering experiments for $k\approx k_H$ confirm this predicted peculiar transition from normal to fast and slow sound.

In addition to the four propagating fast- and slow-sound eigenmodes, $H(k)$ has one diffusive-type eigenmode [cf. Eq. (4.31)] that strongly determines the dynamics of the microscopic concentration c in Fig. 9. The corresponding real eigenvalue $z_c(k)$ behaves as $z_c(k)=D_c k^2$ when $k\rightarrow 0$ (cf. Figs. 11 and 12). We find that the concentration diffusion coefficient $D_c=0.005\ \mathrm{nm}^2/\mathrm{ps}$ is about five times smaller than the Stokes-Einstein diffusion coefficient $D_0=0.0251\ \mathrm{nm}^2/\mathrm{ps}$ discussed in Sec. III D. The reason for this rather unphysical result might be that in our experimental $S(k,\omega)$ we observe mainly the dynamics of the microscopic total number density N of Fig. 9 and not that of c [cf. Eqs. (4.29) and (4.30)]. In fact, the Lorentzian in $S(k,\omega)$ corresponding to $z_c(k)$ has a vanishing amplitude. Thus, the indirect determination of D_c from $S(k,\omega)$ through model fitting (via f_{Nv} and f_{cv} in Fig. 9) and extrapolation to $k\rightarrow 0$ certainly involves large uncertainties. Therefore, our value of D_c is not reliable, and the difference between D_c and D_0 is possibly not significant. It appears that a reliable determination of D_c in mixtures can only be achieved from neutron-scattering experiments for which both $S_{NN}(k,\omega)$ and $S_{cc}(k,\omega)$ in Eq. (4.29) contribute significantly to the total measured $S(k,\omega)$.

Finally, we discuss the relevance of our present results for kinetic theory and light-scattering experiments. Kinetic theory of hard-sphere mixtures representative of dense He-Xe shows the existence of fast and slow sound for $k>k_H$ [2]. Similar to what we find here, fast sound vanishes for $k<k_H$ and slow sound merges into hydrodynamic sound. However, no fast and slow sound is found for $k>k_H$ in a hard-sphere mixture representative of our dense He-Ne state. Thus, for $k>k_H$, microscopic oscillations behave differently for dense mixtures of hard spheres and of soft particles like He or Ne. Such a difference in oscillating behavior is already found between one-component fluids of hard spheres and of soft (Lennard-Jones) particles [see Fig. 5(c) of Ref. 19]. It appears that soft particles oscillate more easily and more pronouncedly than hard spheres.

Light-scattering experiments on dilute-gas mixtures of H_2-Ar [6], H_2-SF_6 [7], H_2-Xe [20] and He-Xe [21] show that, in general, fast sound vanishes for $k<k_H$ and slow sound merges into hydrodynamic sound. Here k_H can be in the experimentally accessible k region. Thus these results are consistent with our present findings from neutron scattering and model fitting (cf. Figs. 11 and 12). It is also shown from light-scattering experiments that the slow-sound lines at $\pm\omega_s^{(2)}(k)$, not directly visible in the measured $S(k,\omega)$, become visible as peaks or shoulders at $\pm\omega_s^{(2)}(k)$ in the related spectrum $\omega^2 S(k,\omega)$.

In Fig. 13 we show $\omega^2 S(k,\omega)$ as a function of ω for our present $He_{0.65}Ne_{0.35}$ state and $k=8\ \mathrm{nm}^{-1}$. Indeed, apart from the main fast-sound peak at $\omega_s^{(1)}(k)$ (solid arrow), one observes a shoulder near $\omega_s^{(2)}(k)$ (dashed arrow). Whether there are side features of $\omega^2 S(k,\omega)$ hidden in the large error bars of Fig. 13 at $\omega>\omega_s^{(1)}(k)$ can only be

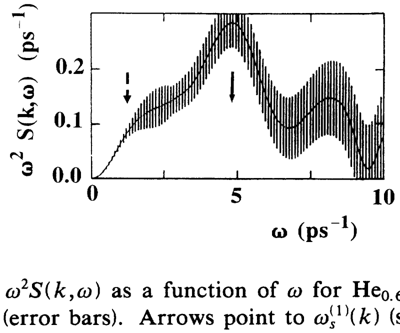

FIG. 13. $\omega^2 S(k,\omega)$ as a function of ω for $He_{0.65}Ne_{0.35}$ and $k=8\ \mathrm{nm}^{-1}$ (error bars). Arrows point to $\omega_s^{(1)}(k)$ (solid arrow, fast sound) and $\omega_s^{(2)}(k)$ (dashed arrow, slow sound). The solid curve connects the midpoints of the error bars.

revealed by neutron scattering with accuracy higher than that used in our present experiment.

APPENDIX

We derive the kinetic equation (4.21) for the set of 25 time correlation functions $G_{jl}(k,t)$ of Eq. (4.19) using the standard Zwanzig-Mori projection operator formalism [22,23,19]. We need the Laplace transforms $\hat{G}_{jl}(k,z)$ of $G_{jl}(k,t)$, defined by

$$\begin{aligned}\hat{G}_{jl}(k,z)&=\int_0^{\infty}dt\, e^{-zt}G_{jl}(k,t)\\ &=\left\langle[\delta a_j(\mathbf{k})]^*\frac{1}{z-L}\delta a_l(\mathbf{k})\right\rangle ,\end{aligned} \tag{A1}$$

with j or $l=c,N,P,T,v$. The Liouville operator L is given by

$$L=\sum_{l=1}^{2}\sum_{q=1}^{N_l}\mathbf{v}_l^{(q)}\cdot\frac{\partial}{\partial\mathbf{r}_l^{(q)}}+\frac{1}{m_l}\mathbf{F}_l^{(q)}\cdot\frac{\partial}{\partial\mathbf{v}_l^{(q)}} , \tag{A2}$$

with $\mathbf{F}_l^{(q)}$ the force exerted on particle q of species l by all other particles,

$$\mathbf{F}_l^{(q)}=-\frac{\partial}{\partial\mathbf{r}_l^{(q)}}\sum_{j=1}^{2}\sum_{p=1}^{N_j}\phi_{lj}(|\mathbf{r}_l^{(q)}-\mathbf{r}_j^{(p)}|) . \tag{A3}$$

The $\hat{G}_{jl}(k,z)$ of Eq. (A1) satisfy the exact Zwanzig-Mori relation

$$z\,\hat{G}_{jl}(k,z)=-\sum_{n=c,N,P,T,v}H_{jn}(k,z)\hat{G}_{nl}(k,z)+\delta_{jl} , \tag{A4}$$

where the symmetric 5×5, k- and z-dependence kinetic matrix $H(k,z)$ is given by

$$H_{jl}(k,z)=-L_{jl}(k)-U_{jl}(k,z) , \tag{A5}$$

with $L_{jl}(k)$ the symmetric Liouville matrix,

$$L_{jl}(k)=\langle[\delta a_j(\mathbf{k})]^*L\,\delta a_l(\mathbf{k})\rangle , \tag{A6}$$

and $U_{jl}(k,z)$ the symmetric matrix of k- and z-dependent transport coefficients,

$$U_{jl}(k,z)=\langle[\delta a_j(\mathbf{k})]^*L\mathcal{P}_{\perp}\frac{1}{z-\mathcal{P}_{\perp}L\mathcal{P}_{\perp}}\mathcal{P}_{\perp}L\,\delta a_l(\mathbf{k})\rangle . \tag{A7}$$

The orthogonal projection operator $\mathcal{P}_{\perp}$ is given by $\mathcal{P}_{\perp}=1-\mathcal{P}$, where $\mathcal{P}$ projects any arbitrary function f on the five basic variables:

$$\mathcal{P}f=\sum_{j=c,N,P,T,v}\delta a_j(\mathbf{k})\langle[\delta a_j(\mathbf{k})]^*f\rangle . \tag{A8}$$

We assume that the z dependence of the transport coefficients in $U(k,z)$ is irrelevant, so that $H(k,z)$ in Eq. (A4) can be replaced by the matrix $H(k)$ with elements

$$H_{jl}(k)=H_{jl}(k,0)=-L_{jl}(k)-U_{jl}(k,0) . \tag{A9}$$

The solution of (A4) then leads, after inverse Laplace transformation, to the relation

$$G_{jl}(k,t)=[e^{-tH(k)}]_{jl} , \tag{A10}$$

which is Eq. (4.21).

For $H(k)$ we need that

$$L\,\delta a_c(\mathbf{k})=if_{cv}(k)\delta a_v(\mathbf{k}) \tag{A11}$$

and that

$$L\,\delta a_N(\mathbf{k})=if_{NP}(k)\delta a_P(\mathbf{k})+if_{Nv}(k)\delta a_v(\mathbf{k}) , \tag{A12}$$

as follows from Eqs. (A2) and (4.10)–(4.16). Here $f_{cv}(k)$, $f_{NP}(k)$, and $f_{Nv}(k)$ are given by Eq. (4.23). The microscopic concentration $\delta a_c(k)$ [cf. Eq. (4.10)] is defined such that on the right-hand side of Eq. (A11) no term occurs proportional to $\delta a_P(\mathbf{k})$. From Eqs. (4.9) and (A8), (A11), and (A12) it follows that

$$\mathcal{P}_{\perp}L\,\delta a_c(\mathbf{k})=\mathcal{P}_{\perp}L\,\delta a_N(\mathbf{k})=0 , \tag{A13}$$

so that in Eq. (A7) $U_{jl}(k,z)=0$ for $j=c$ or N and for $l=c$ or N. Therefore $H(k)$ of Eq. (A9) can be written as

$$H(k)=\begin{bmatrix}0&0&0&0&if_{cv}(k)\\0&0&if_{NP}(k)&0&if_{Nv}(k)\\0&if_{NP}(k)&z_{PP}(k)&if_{PT}(k)&z_{Pv}(k)\\0&0&if_{PT}(k)&z_{TT}(k)&if_{Tv}(k)\\if_{cv}(k)&if_{Nv}(k)&z_{Pv}(k)&if_{Tv}(k)&z_{vv}(k)\end{bmatrix} , \tag{A14}$$

with the transport coefficients ($j=P,T$ or v)

$$\begin{aligned}z_{jj}(k)&=-U_{jj}(k,0) ,\\ z_{Pv}(k)&=-U_{Pv}(k,0) ,\end{aligned} \tag{A15}$$

and the elastic forces

$$\begin{aligned}f_{PT}(k)&=i[L_{PT}(k)+U_{PT}(k,0)] ,\\ f_{Tv}(k)&=i[L_{Tv}(k)+U_{Tv}(k,0)] .\end{aligned} \tag{A16}$$

In Eq. (A15) we use the fact that $L_{jl}(k)=0$ when j and l refer to basic variables that have the same symmetry under microscopic velocity inversion [in particular, $L_{jj}(k)=L_{Pv}(k)=0$]. We find, in a free fit to our experimental results for $S(k,\omega)$, that the cross transport coefficient $z_{Pv}(k)$ in Eq. (A14) is negligible for all k. Thus, Eq. (A14) for $H(k)$ reduces to Eq. (4.22) applied in the main text.

For small k we use the fact that the label $j=c$, N, P, or T refers to a hydrodynamic (conserved) variable, the time evolution of which behaves near $k=0$ as $L\delta a_j(\mathbf{k})\sim k$. Therefore the forces $f_{PT}(k)\sim f_{Tv}(k)\sim k$ vanish proportional to k and the transport coefficients $z_{PP}(k)\sim z_{TT}(k)\sim k^2$ proportional to k^2. The transport coefficient $z_{vv}(k)$ approaches a constant $z_{vv}(0)$ for $k\rightarrow0$, since $\delta a_v(\mathbf{k})$ is a kinetic (nonconserved) variable.

*Present address: AECL Research, Chalk River Laboratories, Chalk River, Ontario, Canada KOJ 1J0.

[1] A. Campa and E. G. D. Cohen, Phys. Rev. Lett. **61**, 853 (1988).

[2] A. Campa and E. G. D. Cohen, Phys. Rev. A **41**, 5451 (1990).

[3] J. Bosse, G. Jacucci, M. Ronchetti, and W. Schirmacher, Phys. Rev. Lett. **57**, 3277 (1986).

[4] W. Montfrooij, P. Westerhuijs, and I. M. de Schepper, Phys. Rev. Lett. **61**, 2155 (1989).

[5] W. Montfrooij, P. Westerhuijs, V. O. de Haan, and I. M. de Schepper, Phys. Rev. Lett. **63**, 544 (1989).

[6] G. H. Wegdam, A. Bot, R. P. C. Schram, and H. M. Schaink, Phys. Rev. Lett. **63**, 2697 (1989).

[7] M. J. Clouter, H. Luo, H. Kiefte, and J. A. Zollweg, Phys. Rev. A **41**, 2239 (1990).

[8] W. Montfrooij, L. A. de Graaf, and I. M. de Schepper, Phys. Rev. A **44**, 6559 (1991).

[9] H. N. W. Lekkerkerker and W. G. Laidlaw, Phys. Rev. A **9**, 346 (1974).

[10] V. V. Sychev, A. A. Vasserman, A. D. Kozlov, G. A. Spiridonov, and V. A. Tsymarny, *Thermodynamic Properties of Helium* (Springer-Verlag, Berlin, 1987).

[11] P. Verkerk and A. A. van Well, Nucl. Instrum. Methods **228**, 438 (1985).

[12] N. K. Ailawadi, Phys. Rep. **57**, 341 (1980).

[13] E. G. D. Cohen and I. M. de Schepper, J. Stat. Phys. **63**, 241 (1991).

[14] P. N. Pusey, H. N. W. Lekkerkerker, E. G. D. Cohen, and I. M. de Schepper, Physica A **164**, 12 (1990).

[15] H. M. Fijnaut, C. Pathmamaharan, E. A. Nieuwenhuis, and A. Vrij, Chem. Phys. Lett. **59**, 351 (1978).

[16] C. Y. Ho, *Properties of Nonmetallic Fluid Elements* (Hemisphere, New York, 1989).

[17] U. K. Deiters, Fluid Phase Equilibria **33**, 267 (1987).

[18] C. K. Heck and P. L. Barrick, Adv. Cryogenic, Engr. **12**, 714 (1967).

[19] I. M. de Schepper, E. G. D. Cohen, C. Bruin, J. C. van Rijs, W. Montfrooij, and L. A. de Graaf, Phys. Rev. A **38**, 271 (1988).

[20] R. P. C. Schram, A. Bot, H. M. Schaink, and G. H. Wegdam, J. Phys. Condens. Matter **2**, SA157 (1990).

[21] G. H. Wegdam and H. M. Schaink, Phys. Rev. A **40**, 7301 (1989).

[22] N. K. Ailawadi, A. Rahman, and R. Zwanzig, Phys. Rev. A **4**, 1616 (1971).

[23] R. D. Mountain, *Advances in Molecular Relaxation Processes* (North-Holland, Amsterdam, 1976), Vol. 9, p. 225.